Influence of many-body effects on hole quasiparticle dynamics in a WS_2 monolayer

Fabio Bussolotti,[1,*] Jing Yang,[2] Hiroyo Kawai,[2] Jing Yee Chee,[1] and Kuan Eng Johnson Goh[1,3,†]

[1]*Institute of Materials Research & Engineering (IMRE), A*STAR (Agency for Science, Technology, and Research), 2 Fusionopolis Way, Innovis, Singapore 138634, Singapore*

[2]*Institute of High Performance Computing, Agency for Science, Technology and Research, 1 Fusionopolis Way, #16-16 Connexis, Singapore 138632, Singapore*

[3]*Department of Physics, National University of Singapore, 2 Science Drive 3, Singapore 117542, Singapore*

(Received 4 August 2020; revised 18 November 2020; accepted 22 December 2020; published 13 January 2021; corrected 11 October 2021)

Monolayer (ML) transition metal dichalcogenides (TMDCs) emerged as ideal materials to combine spin and momentum of charge carriers for spintronics and valleytronics applications. Despite its relevance for TMDC-based technology, the impact of the various many-body-like interactions of charge carriers with defects, phonons, and other system's quasiparticles on the charge dynamics and transport properties remains experimentally elusive, being commonly overshadowed by the strong ML interactions with other materials (such as substrate and contacts) introduced in standard experimental approaches. Here, a method combining interface engineering and angle-resolved photoemission spectroscopy (ARPES) enables a direct investigation of the impact of many-body effects on the hole quasiparticle dynamics of WS_2 ML on graphite and extraction of relevant transport parameters. In particular, at the valence band edge, a clear ARPES line-shape asymmetry is observed, mainly reflecting the hole interaction with intralayer electrons and defects while a negligible hole-phonon coupling is found. Using the valley hole quasiparticle lifetime and effective mass extracted from ARPES data at different temperatures, we estimated a hole mobility of $\sim 300\,\mathrm{cm^2\,V^{-1}\,s^{-1}}$, comparable to some of the highest values reported by transport measurements.

DOI: 10.1103/PhysRevB.103.045412

I. INTRODUCTION

In semiconducting transition metal dichalcogenide (TMDC) monolayers (MLs) [MX_2, where $M =$ Mo, W, and $X =$ S, Se; see Figs. 1(a) and 1(b)] the lack of in-plane inversion centers combined with a strong spin-orbit coupling in the metal atoms leads to energy splitting near the valence and conduction band edges (K valleys) at the corner of the hexagonal Brillouin zone (BZ) [Fig. 1(c)], with a concurrent lifting of the spin degeneracy [1]. Time-reversal symmetry also requires opposite spin polarization in opposite momentum valleys [K, K'; see Fig. 1(c)], resulting in a spin-valley coupling relationship [1,2] which allows, for example, the selective excitation of carriers at specific valleys via the helicity of incoming circularly polarized light [3–5]. This unique "spin locking" mechanism at the band edges, where charge carriers are located [6], promotes TMDC MLs as the most suitable candidates for combining charge transport with spin and valley degrees of freedom in spintronics and valleytronics applications [7,8]. A detailed understanding of the valley charge carrier (and coupled spin) dynamics in TMDC MLs and the related impact on critical device parameters such as charge lifetimes and mobilities is therefore crucial to fully exploit their technological potentials.

The study of such carrier dynamics typically required full fabrication of TMDC-based transistors and the analysis of the transport characteristics [9–15]. Device properties are however strongly affected by charge trapping processes at the interface of TMDC MLs with the supporting substrate [9] as well as the metallic electrodes [10,11,16] and these effects are difficult to be fully mitigated and/or eliminated during the device fabrication steps. Consequently, the reported transport properties may vary largely even for a *specific* material [9,11] under comparable experimental conditions [9,11] (i.e., temperature, metal contacts, supporting substrate). These problems significantly complicate our understanding of many-body processes, i.e., interactions of charge carriers with lattice vibrations (phonons), defects, and other charges within the two-dimensional (2D) layer. They also limit our ability to extract related transport parameters.

Thanks to its energy/momentum detection capability, angle-resolved photoemission spectroscopy (ARPES) can provide an alternative, direct access route to the electronic properties at the band edges of metallic and semiconducting materials. In this context, ARPES was successfully applied to investigate the charge scattering and relaxation in a variety of layered materials via the observation of anomalous change in the energy dispersion [17] and/or the photoemission peaks' width [18–20]. However, despite their strong importance for device optimization these phenomena are not commonly investigated in much detail in ARPES studies of TMDC MLs due to a number of fabrication and technical limitations. For exfoliated, micrometer-sized MLs mechanically

*b.fabio@imre.a-star.edu.sg
†kejgoh@yahoo.com; gohj@imre.a-star.edu.sg

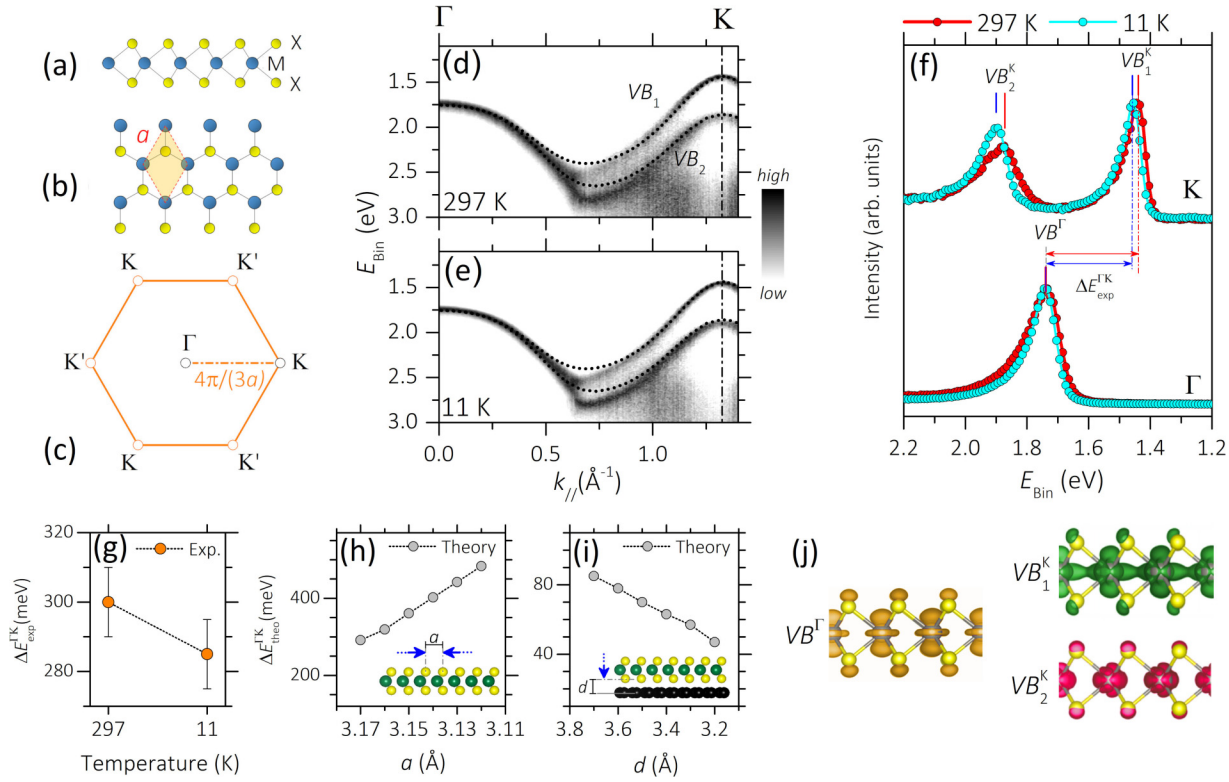

FIG. 1. Structure and temperature-dependent band dispersion of WS_2 ML on HOPG substrate. (a), (b) Schematic of TMDC ML (MX_2) at side (a) and top view (b). Shaded area in (b) indicates the unit cell, with the corresponding lattice parameter a. (c) Brillouin zone (BZ) of TMDC ML with inequivalent K, K' valleys. (d), (e) ARPES intensity plot (normalized to maximum) showing the valence band dispersion of WS_2 ML along ΓK high symmetry direction [dash dotted line in (c)] at 297 K (d) and 11 K (e). The splitting into two well-distinguished subbands (VB_1 and VB_2) is clearly visible and well reproduced by band structure calculation for freestanding WS_2 ML [dotted black curves in (d),(e)]. (f) EDCs at Γ and K point (intensity normalized to maximum) at 297 and 11 K. The positions of peak maxima (VB^{Γ}, VB_1^K, VB_2^K) are indicated by vertical bar. The energy separation between the band extrema at the Γ and K points ($\Delta E_{exp}^{\Gamma K}$) is also indicated. (g) Experimental $\Delta E_{exp}^{\Gamma K}$ as extracted from peak maxima position in (f), as evaluated by peak fitting of EDCs (see main text). (h),(i) Calculated $\Delta E_{theo}^{\Gamma K}$ as a function of the layer-substrate distance d [(h); see inset] and the in-plane lattice constant a [(i); see inset] of a freestanding ML (see text for more details). (j) Calculated charge density of valence band states at Γ point (VB^{Γ}) and local maxima at K point (VB_1^K, VB_2^K).

transferred on thin oxide substrates, the ARPES data are typically too broad in energy to allow a detailed photoemission line-shape analysis, due to the relatively high amount of structural and chemical defects in fabricated layer/substrate interfaces as well as the limited energy resolution of the required micro-ARPES techniques [21,22]. Large-scale, higher quality TMDC-based interfaces can be obtained via epitaxial deposition on doped or metallic single crystal substrate [23–27], but in this case the strong interaction with the conductive substrate significantly affects the electronic band structure of the layer [23–27] and also obscure signatures of the *intrinsic* charge dynamics on the ARPES line shape [25,26].

In this work we report an ARPES study of the electronic properties of WS_2 ML interfaced with graphite substrate. The weak layer-substrate interaction, ensured by a mechanical transfer procedure combined with the intralayer localization of electronic states at the valence band edge, facilitates a direct access of valley hole quasiparticle (and locked spin) dynamics in the WS_2 ML. Our data reveals a clear asymmetry in the photoemission line shape of valence band valley point. By temperature-dependent measurements, this peculiar spectral feature was analyzed and attributed to valley hole interaction with intralayer electrons and defects while negligible hole-phonon coupling was found. These results have major implications on the charge (and valley-locked spin) transport mechanism in semiconducting TMDCs ML. In particular, we observe a nearly temperature-independent hole mobility, readily estimated from the line-shape and band dispersion analysis, and in good agreement with transport studies of TMDC MLs.

II. EXPERIMENTAL RESULTS

A. Engineering of WS_2 ML-substrate interaction

A WS_2 ML was grown ($\sim 2 \times 2\,mm^2$) onto an insulating sapphire (0001) surface via epitaxial deposition (see the Appendix). The as-obtained single-crystal TMDC film was then mechanically transferred on a conductive highly ordered pyrolytic graphite (HOPG) to prevent sample charging during ARPES acquisition [see Sec. S1 and Fig. S1 in the Supplemental Material (SM) [28] for ARPES experimental details [8,29,30]]. Optical images of the WS_2 layer before and after the transfer on the HOPG are shown in Figs. S2(a) and S2(b) of the SM [28,31–33]. The quality of the

as-prepared TMDC/HOPG interface was directly assessed by preliminary ARPES measurements [Figs. S2(c)–S2(f) and x-ray photoelectron (XPS) spectroscopy study (Fig. S3) in the SM [28,34–37]] suggesting a limited amount of structural disorder and chemical defects [37,38].

Figures 1(d) and 1(e) present the ARPES intensity plots of the WS_2 ML on HOPG at 297 K (d) and 11 K (e) as a function of the binding energy (E_{Bin}) and in-plane momentum component ($k_{//}$) along the ΓK direction of the WS_2 BZ. Two valence band branches (VB_1 and VB_2) are clearly resolved, originating from the strong spin-orbit coupling effect in the WS_2 ML [1]. At both temperatures, experimental data are well reproduced by the calculated ΓK dispersion for isolated MLs [short dotted curves in Figs. 1(d) and 1(e)] within the limit of first principles band structure calculations (see the Appendix and Sec. S4 in the SM [28] for details) thus also suggesting a nearly free-standing nature of the WS_2 ML on the HOPG substrate. Band dispersion at 11 K, however, also shows a slight change with respect to the 297-K data. This is evident in the comparison of the ARPES energy distribution curves (EDCs) at Γ and K points [Fig. 1(f)] and whose peak positions (VB_1^{K}, VB_2^{K}, and VB^{Γ}) shift differently upon sample cooling. Consequently, the binding energy separation between the local valence-band maxima at the Γ and K points [$\Delta E_{\mathrm{exp}}^{\Gamma\mathrm{K}}$; Fig. 1(f)] decreases from ∼300 to ∼280 meV [Fig. 1(g)], to reveal a slight valence band distortion across the BZ.

In principle, the above results can be rationalized by a combination of in-plane lattice constant a [Fig. 1(h)] and layer-substrate distance d [Fig. 1(i)] contraction upon cooling. Both mechanisms reflect the expected structural modifications of materials when their temperature changes [39–42] and they were previously reported to modify the electronic and optical response of TMDC multilayers and based heterostructures [39,43,44]. The impact of the temperature on the WS_2 ML band dispersion was discussed by calculating the energy difference between the valence band positions at the Γ and K point ($\Delta E_{\mathrm{theo}}^{\Gamma\mathrm{K}}$) as a function of the relevant structural parameters a and d (see also Sec. S4 and Fig. S4 in the SM [28] and also Refs. [45,46]). In a free-standing WS_2 ML a contraction of the in-plane lattice constant a that occurs at lower temperature leads to an increase of the $\Delta E_{\mathrm{theo}}^{\Gamma\mathrm{K}}$ value [Fig. 1(h)] in contrast to our experimental results [Fig. 1(g)]. However, when the substrate presence is considered [Fig. 1(i)] the contraction of the layer-substrate distance d induces a gradual decrease of $\Delta E_{\mathrm{theo}}^{\Gamma\mathrm{K}}$, consistently with the experimental band distortion. These results indicate that the reduction of the layer-substrate distance d could be a dominant factor for the observed valence band change. A shorter WS_2-HOPG distance can favor charge transfer/hybridization phenomena as well as electrostatic screening effect (scaling as $1/d$ [6]) between TMDC and substrate electronic state with consequent impact on the valence band binding energy. This effect is determined by the different wave function's spatial extension at various regions of the TMDC BZ, i.e., in plane at the K point (VB_1^{K}, VB_2^{K} states) and out of plane at the Γ point (VB^{Γ} state) [Fig. 1(j)]. Here, a larger layer-substrate interaction is expected [21] which then results in the observed $k_{//}$-dependent binding energy shift.

Temperature-controlled valence band distortion was also reported in our previous ARPES studies on MoS_2 ML on HOPG [30], as prepared by using similar mechanical transfer methods, thus indicating a general approach for the fine control of the layer-substrate interaction in TMDC-based heterostructures for fundamental studies. With respect to the direct deposition on the supporting substrate the mechanical transfers of TMDCs, as utilized in the present study, were reported to reduce the layer-substrate interaction [21]. This, combined with the essential "immunity" of the intralayer localized valence band states at the K point from interfacial potential variation, offers a unique platform for the direct ARPES probe of the intrinsic TMDCs' electronic properties.

B. ARPES line-shape analysis

Figures 2(a) and 2(b) show the EDCs around the K point for 297 K (a) and 11 K (b), after Shirley-type inelastic background subtraction (Sec. S5, Fig. S5, in the SM [28]) [34,47–49]. The binding energy scale (E_{Bin}) was aligned to the position of the highest point of each EDC ($E_{\mathrm{Bin}}^{\mathrm{max}}$). Even after background subtraction and thanks to the large spin-orbit splitting (∼0.45 eV) with respect to the intrinsic peak width (∼0.1 eV), a clear asymmetry in the EDC line shape is resolved. It is noteworthy that this asymmetry was not observed in previous ARPES studies of high quality TMDC MLs deposited on single-crystal metals where a fully symmetric line shape is constantly reported [25,26,33].

In principle, electron removal by photoemission is expected to leave the 2D system in a *fully relaxed* hole quasiparticle state [19,47]. A single photoemission peak should therefore be observed, whose binding energy position and width reflect the main hole-quasiparticle band energy and dynamics. However, the hole interaction with other electrons in the system and/or with lattice vibrations (hole-phonon coupling) can also result in a number of *partially relaxed* (i.e., excited) final photoemission states [19,47]. In a system of N-interacting electrons the hole created upon photoemission corresponds to a sudden change of potential and therefore of the system Hamiltonian. Therefore, the wave function of the $N-1$ electrons before photoemission (i.e., initial states) is no longer adequate for their description after the hole creation ("$N-1$" electrons $+1$ photoelectron) in the final state. According to the transition rule multiple final states configuration can exist, each of them contributing to the total photoemission signal [19,47]. These secondary excitations can contribute to the overall spectral intensity with a series of satellite peaks located at the higher binding energies (i.e., low kinetic energy) of the main hole quasiparticle peak, thus resulting in the EDCs' line-shape asymmetry [19,20,50]. More generally, the position and energy broadening of each satellite components reflects the details of the corresponding many-body excitation [19,20,50] (see Sec. S6 in the SM [28] for additional discussion).

In this context, the experimental EDCs at the K point were fitted by a series of symmetric, equally spaced Voigt functions according to the details described in the Appendix, in order to reproduce the main quasiparticle peak [VB_1^{K} and VB_2^{K} components, continuous curves (brighter shading) in Figs. 2(a) and 2(b)] and line-shape asymmetry [c_1, c_2, c_3 components, dotted curves (darker shading) in Figs. 2(a) and 2(b)] in the ARPES data.

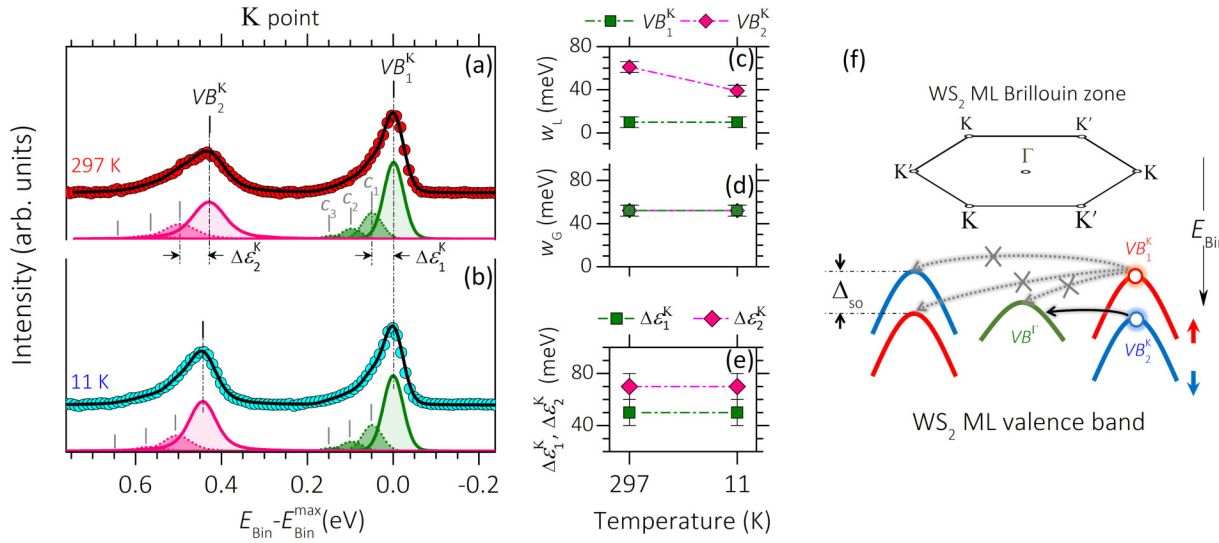

FIG. 2. Temperature dependence of EDC line shape at K valley. (a), (b) Experimental EDCs at K point (closed circles, background subtracted) for 297 K (a) and 11 K (b) with corresponding peak fitting results. The energy position of the main VB_1^K and VB_2^K (continuous curves with bright shadings) and satellite fitting components (dotted curves with dark shadings) are indicated by vertical bars. The energy separation ($\Delta\varepsilon_1^K$, $\Delta\varepsilon_2^K$) between the peak components are shown for the 297-K data in (a) (see main text for details). The notation of the satellite components (c_1, c_2, c_3) is omitted in (b) for clarity. The binding energy scale (E_{Bin}) was aligned to the position of the VB_1^Γ peak (E_{Bin}^{max}). (c)–(e) Values of w_L (c) and w_G (d) of VB_1^K and VB_2^K components and corresponding peak energy separation $\Delta\varepsilon_1^K$, $\Delta\varepsilon_2^K$ (e) as extracted from the data fitting in (a) and (b). (f) Schematic of allowed (continuous black arrows) and forbidden (dash dotted grey arrows) phonon-mediated hole relaxation process at the K valley of WS_2 valence band (see text for detailed discussion). The valence band at K and $K\prime$ of the ML BZ are spin split (energy separation $= \Delta_{SO}$) with the color (red, blue) indicating the opposite spin direction (also marked by thick vertical arrows). The valence band at Γ is spin degenerate (green curve).

At both temperatures, a Lorentzian width of $w_L = 10$ meV, directly related to the hole quasiparticle lifetime via uncertainty principle [47], was measured for the VB_1^K peak [Fig. 2(c)]. In the same temperature range, the w_L value of the VB_2^K peak changes significantly from 62 to 39 meV [Fig. 2(c)]. No detectable change in the Gaussian broadening of the VB_1^K and VB_2^K components ($w_G = 52$ meV) is observed [Fig. 2(d)], with these values reflecting the impact of finite experimental resolution and intralayer and interfacial defects on the peak energy broadening [20,47,51]. Analogous temperature stability is found for the peak energy separations at both the spin-orbit valence band branches, i.e., $\Delta\varepsilon_1^K = 50$ meV and $\Delta\varepsilon_2^K = 70$ meV [Fig. 2(e)].

The increase of layer-substrate interaction at low temperature is expected to reduce the hole quasiparticle lifetime by favoring the ML-HOPG charge transfer/hybridization process as well as via larger substrate electrostatic screening [25,26,33]. This effect should lead to an increase of the w_L peak width upon cooling from 297 to 11 K, in contrast to our experimental results for the VB_1^K and VB_2^K component [Fig. 2(c)]. As pointed out in the previous section, such "immunity" of valley hole quasiparticle (and locked spin) lifetime with respect to layer-substrate potential changes reflects the strong in-plane localization of the valence band states at the K point, which limits the impact of the interfacial potential landscape on the hole quasiparticle relaxation and lifetime [30]. The intralayer localization of the valence band valley states can also suppress the contribution of the interface defects and related Coulomb potential [51] to the overall Gaussian broadening of EDCs even at 11 K, when the layer substrate distance is reduced. The w_G values extracted at the K point for the VB_1 and VB_2 band branches [$w_G = 52$ meV, Fig. 2(d)] is therefore mainly determined by finite instrumental resolution (~20 meV; see the Appendix) and energy broadening introduced by *temperature independent* defect scattering [19].

The absence of any Lorentzian width changes upon temperature for the VB_1^K state at the K point [Fig. 2(c)] is in line with theoretical expectation for single-layer WS_2, assigning a negligible contribution of hole-phonon coupling effect to the hole quasiparticle lifetime at the TMDC valence band edge [25,52]. A schematic of the allowed and forbidden vibration mediated hole-scattering process in illustrated in Fig. 2(f). For both temperatures that we measured experimentally, no phonon-mediated hole scattering from the K to the Γ point is possible as the thermal energy (<25 meV) is much smaller with respect to the hole energy barrier between the Γ state and the K point [~300 meV; see Figs. 1(d)–1(f)]. Hole scattering to $VB_2^{K'}$ states at the opposite K' valley is also limited by the energetic barrier introduced by the large spin orbit splitting [0.45 eV at the K point; Fig. 2(f)]. Despite the energetic possibility, hole scattering from the K to K' valley would require a *simultaneous spin flip* in addition to a large momentum transfer [Fig. 2(f)] and is therefore expected to be a low probability event [52]. High binding energy peaks resulting from hole-phonon coupling effects were previously observed in the ARPES line shape of 2D layered materials [20,50], their relative intensity, and energy separation depending on the coupling strength and vibration energy, respectively. For the VB_1 band at the K point, however, the negligible hole-phonon coupling would quench any high binding energy components, in contrast to the clear line-shape asymmetry observed in our ARPES data [Figs. 2(a) and 2(b)]. As such, the ARPES line

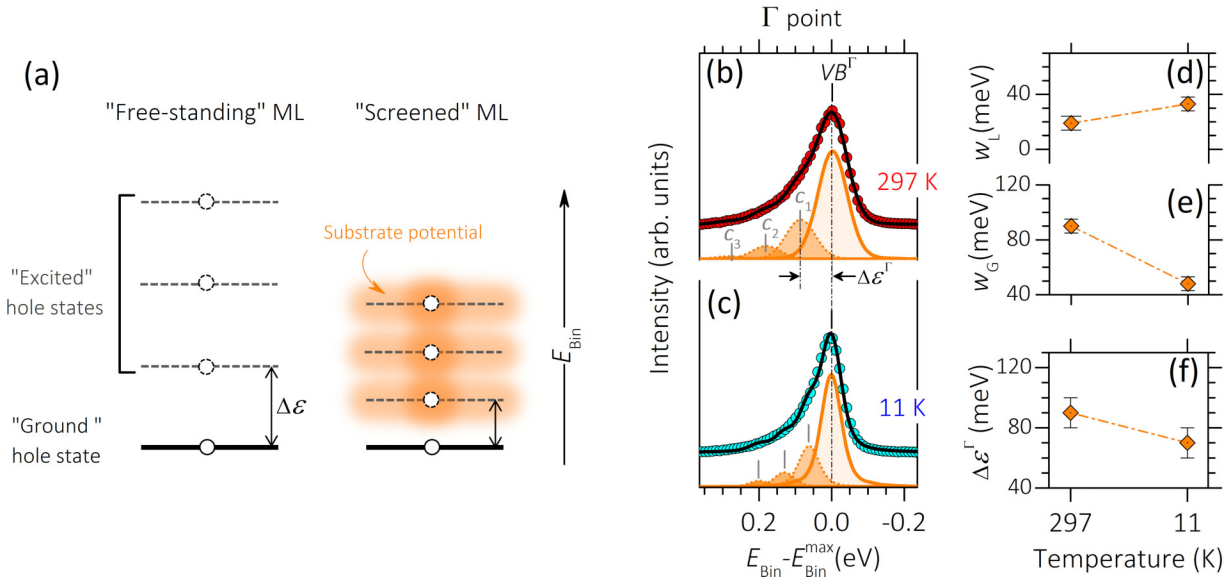

FIG. 3. Hole quasiparticle energy vs layer-substrate interaction and temperature dependence of EDC line shape at Γ points. (a) Schematic showing multiple excitation processes in free standing ML and under substrate potential screening effect. $\Delta\varepsilon$ indicates the energy separation between the ground and excited hole states (b), (c). Experimental EDCs at *K* point (closed circles, inelastic background subtracted) for 297 K (b) and 11 K (c) with corresponding peak fitting results. The energy position of the main (VB^{Γ}, continuous curves with bright shading) and satellite fitting components (dotted curves with dark shading) are indicated by vertical bars. The energy separation ($\Delta\varepsilon^{\Gamma}$) between the peak components are shown for the 297-K data in (b) (see main text for details). The notation of the satellite components (c_1, c_2, c_3) is omitted in (c) for clarity. The binding energy values (E_{Bin}) was aligned to the position of the VB^{Γ} peak (E_{Bin}^{max}). (d)–(f) Values of w_L (d) and w_G (e) of VB^{Γ} components and corresponding peak energy separation $\Delta\varepsilon^{\Gamma}$ (f) as extracted from the data fitting in (b) and (c).

shape and width observed at the WS_2 ML valence band edge, and the related hole quasiparticle dynamics, can be ascribed to intralayer many-body relaxation as mediated by *temperature-independent* electrons and defect scattering [19]. In particular the latter, mainly originating from *S* vacancies introduced during the CVD process (see discussion in SM Sec. S3), can reduce the hole quasiparticle lifetime and therefore increases the Lorentzian width of the main and satellite peaks in the measured EDC signal.

In contrast, as the VB_2^K valley state is located at higher binding energy with respect to the valence band state at Γ point [Figs. 1(d)–1(f)], phonon-mediated hole scattering between the *K* and Γ point of the BZ are then allowed at 297 K [Fig. 2(f)]. This reduces the lifetime with respect to the VB_1^K hole quasiparticle state, which also explains the corresponding difference in w_L values with respect to the VB_1 band [62 meV of VB_2^K vs 10 meV of VB_1^K; Fig. 2(c)]. At 11 K, vibrational scattering is quenched and therefore a reduction of the VB_2^K peak Lorentzian width w_L is observed [from 62 to 39 meV; Fig. 2(c)], reflecting the increase in the hole lifetime. Even if hole scattering can be mediated by optical phonons, their maximum energy (∼20 meV) [52,53] does not correspond to the peak energy separation (70 meV), in contrast to the predictions of the vibrational model. Therefore, the overall asymmetry of the VB_2 band at the *K* point also appears to be similarly dominated by the intralayer many-body processes.

The mutual charge interaction in 2D semiconductors is highly sensitive to the details of local potential environment, as mainly determined by the presence of supporting substrate [54]. Radja *et al.* recently showed the reduction of the energy separation between exciton quasiparticle states in TMDC ML with increasing substrate dielectric screening, scaling up with the substrate (multilayer graphene) thickness [55]. In the present case, as the in-plane valence band valley states are "protected" from the interfacial potential landscape, its temperature induced changes have nearly no impact on the energy of the secondary hole quasiparticle excitations with respect the ground hole states, thus qualitatively explaining the temperature stability of $\Delta\varepsilon_1^K$ and $\Delta\varepsilon_2^K$ values at the *K* point [Fig. 2(e)].

According to the above model, a larger layer-substrate integration leads, via charge transfer/hybridization or dielectric screening, to a progressive reduction of the energy separation between the main and satellite components [see schematic in Fig. 3(a)] and, therefore, to the overall peak line-shape asymmetry. This is the reason why, in contrast to our observations of asymmetric line shapes of WS_2 ML, fully symmetric ARPES peaks were commonly observed at the *K* point of single crystal TMDCs grown on metals [25,26], where a much larger substrate-layer interaction and electrostatic screening effects are established (see Fig. S7 in the SM for a representative comparison with previously reported ARPES data). Other works [56,57] using insulating substrates (e.g., hBN) were not able to resolve such line-shape asymmetry at the *K* valley region perhaps due to significant peak broadening (∼0.3 eV [56]) or poor signal-to-noise ratio in the data [57].

Evidence of the substrate-layer interaction reducing peak line-shape asymmetry can be seen in the valence band EDCs at Γ (see the Appendix), where the electronic wave function spatially extends in the out-of-plane direction [Fig. 1(j)] and a line-shape asymmetry is also observed [Figs. 3(b) and 3(c)]. The change of the main peak (VB^{Γ}) widths [w_L, w_G, see

Figs. 3(d) and 3(e)] upon cooling are compatible with a weak but shorter layer-substrate interaction leading to a larger hole lifetime [w_L increases from 18 to 32 meV; Fig. 3(d)] and improved screening of the Coulomb disorder [w_G decreases from 90 to 48 meV, Fig. 3(e)] from interface defect/impurities, as reported in previous ARPES studies of layered materials [51]. A significant reduction of the peak energy separation ($\Delta\varepsilon^{\Gamma}$) from 90 to 70 meV is also consistently observed, thus leading to a reduction of the overall line-shape asymmetry [Fig. 3(f); see also Sec. S6 and Fig. S6 in the SM [28] for additional analysis]. Interestingly, in Ref. [57] a slight asymmetry is visible in the EDC data at the Γ point of WS_2(ML)/hBN. The ARPES line shape is however not discussed in detail and was attributed to background effects. For our WS_2(ML)/HOPG interface, the latter interpretation is excluded, as discussed in Sec. S6 of the SM.

We note that the reported EDC energy shift and line-shape modification are fully reversible upon recovery of the 297 K [see SM Fig. S9(a)] as well as independent on the probed area of the sample as verified by data acquisition on a different sample position [Fig. S9(b)].

Finally, we note that work function inhomogeneities due to the intrinsic defects and thickness of the HOPG substrate for different domains under the probed sample area may in principle lead to a replica at different binding energies of the main hole quasiparticle peaks [37,58]. In this case, however, the energy separation of the various peak components (i.e., $\Delta\varepsilon^{\Gamma}$, $\Delta\varepsilon_1^{K}$, $\Delta\varepsilon_2^{K}$) from the main quasiparticle peak should be the same at both the *K* and Γ points since the Fermi level shift in the gap due to work function change is independent on the electron momentum. This contrasts for example with the different separations found from our data fitting at room temperature showing $\Delta\varepsilon^{\Gamma} = 90$ meV, $\Delta\varepsilon_1^{K} = 70$ meV and $\Delta\varepsilon_2^{K} = 50$ meV [Figs. 2(e) and 3(f)]. Energy separation between the various peak components at the Γ point should also be temperature independent, as local change of the work function is driven by local Fermi level pinning effect at the layer substrate interface [59]. This is also in contrast with our results showing a $\Delta\varepsilon^{\Gamma}$ reduction from 90 to 70 meV upon cooling from 297 to 11 K [Fig. 3(f)]. Moreover, even in the case of temperature dependent work function changes, the energy separation between peak components should be similarly affected at both the Γ and *K* points which is in contrast to our observations [Figs. 2(e) and 3(f)].

C. Estimation of the valley hole mobility

Figures 4(a) and 4(b) show the experimental VB_1 band dispersion (closed circles) around the *K* point of WS_2 ML at 297 K (a) and 11 K (b). The valley hole effective mass m^* was obtained by parabolic fitting of the experimental data (continues curves). Details on the band dispersion evaluation and peak fitting procedure are reported in the Appendix. At both temperatures, a value of $m^* = (0.34 \pm 0.05)m_0$ was found (see Appendix), where m_0 is the electron mass, in good agreement with previous ARPES findings [33]. The absence of temperature dependence is consistent with the negligible interface and vibrational effects on the VB_1 valence band at the valley point (see above discussion), with the hole quasiparticle dynamics being mainly dominated by interaction with

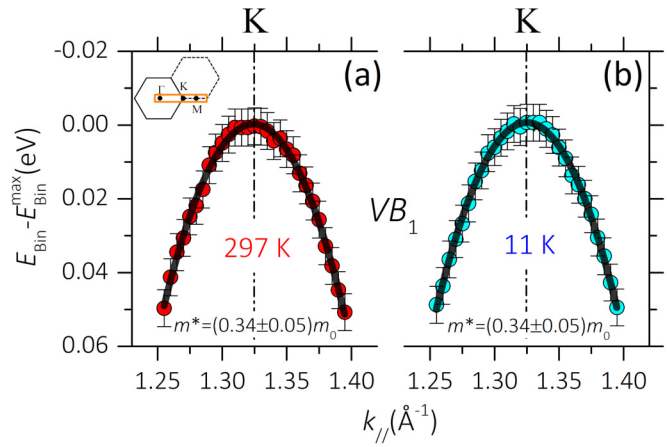

FIG. 4. Valley hole effective mass. (a), (b) Experimental valence band dispersion around *K* valley as extracted from the EDC analysis at 297 K (a) and 11 K (b), with corresponding parabolic fitting. The binding energy values (E_{Bin}) was aligned to the position of the maximum of the fitting curve, where *K* point is exactly located. The hole effective mass m^* at the valence band maxima was extracted from the curvature of the fitting curve at 297 and 11 K and the corresponding values reported in (a) and (b), respectively (see text for details). The high symmetry points of the first BZ (Γ,*K*) (black hexagon) and second BZ (*M*) (dotted hexagon) are shown. The orange rectangle defines the momentum scanning direction (see Appendix for more details).

intralayer electrons and defects. In the same temperature range a hole lifetime of $\tau = (65 \pm 35)$ fs can be directly estimated from the Lorentzian peak width of the VB_1 quasiparticle peak via the uncertainty principle ($w_L = 10 \pm 5$ meV; see the Appendix and also Sec. S8, Fig. S8, in the SM [28] for details on w_L estimation). A first order estimate of the hole mobility (μ) can be obtained in the framework of the Drude model as $\mu = e\tau/m^*$, [6], with e being the electron charge. For our WS_2 ML, a temperature-independent hole mobility of $\mu = (340 \pm 220)$ cm^2/V s is obtained. We note that the relaxation time here is actually the spectral lifetime and not the transport lifetime, where a velocity term weighting forward/backward scattering [60] would need to be included for more accuracy estimates. In Ref. [60] the relation between spectral and transport lifetime was theoretically explored and although the authors concluded that a direct relation between the two lifetimes cannot be easily obtained they found that on average the transport relaxation time may differ only slightly from its spectroscopic counterpart, while the changes around a specific region of momentum space can vary by up to 20% [60]. Within the limit of our approximation, the extracted mobility value for WS_2 is in line with the highest hole values reported in transport studies on TMDC based devices [11] although we note that to the best of our knowledge a direct hole transport mobility in WS_2 ML is yet to be reported. For WSe_2 ML, however, having a comparable valley hole effective mass ($\sim 0.4m_0$) [61], a mobility value of ~ 200 cm^2/V s with a very weak temperature dependence in 5–300 K was reported [13]. These results also indicate the negligible impact of phonon scattering on the valley hole carrier in the WSe_2 ML, thus confirming the validity of our ARPES based approach

to obtain information on the transport properties in TMDC materials.

III. DISCUSSION

The clear valence band line-shape asymmetry in Fig. 3 is the manifestation of intralayer many-body effects. Such a peculiar spectral feature is not commonly observed in previous ARPES studies on TMDC MLs deposited on single crystal metals [25,26], a result we assign to the weak substrate-layer interaction and electrostatic screening effects in our system. We note that an analogous asymmetric photoemission line shape was observed in a core level signal of metallic systems [62,63]. In such systems, the origin of the line-shape renormalization from a fully symmetric core level peak was attributed to many-body interactions of the metallic conduction electrons at Fermi level with the localized deep energy hole [62,63]. No asymmetry is therefore expected in the ARPES signal of delocalized valence bands states of semiconducting material, having zero density of states at the Fermi level. Our experimental findings reveal a different picture, indicating the possibility of similar line-shape renormalization phenomena in the low energy bands of 2D semiconductor. Qualitatively this process can reflect the well-known reduced intralayer electrostatic screening of TMDC MLs, already responsible of the large exciton binding energy (0.3–0.8 eV) [55,64] detected in optical measurements, and can favor the interaction of photoemission hole with surrounding electron in the valence bands. A more sophisticated approach involving detailed spectral function calculation is however required for a quantitative description of the above experimental results.

At the valence band edge, the hole quasiparticle dynamics are also found to be unaffected by vibrational scattering, being strongly limited by both energetic and spin restrictions. The results are consistent with theoretical studies on hole-phonon coupling in TMDC MLs [52]. In addition they suggest that holes, rather than electrons, are advantageous as free carriers to encode and transport information in a valleytronics device. The conduction band splitting at the valley point of TMDCs (∼1–10 meV) is in fact much smaller with respect to the valence band (∼100 meV). The small conduction band splitting implies that the inequivalent K and K' valleys are susceptible to phonon-mediated intervalley scattering, thus limiting the retention time of information encoded in the conduction valley state [52]. We note that the current use of electrons as free carriers in a TMDC ML based device is essentially driven by state-of-the-art of contact fabrication technology, as chemical disorder and Fermi level pinning at the ML/metal interface determines a low electron injection barrier [11]. Recent progress in low-damage contact fabrication opens the route to a more systematic investigation of hole based devices [11]. In addition, to reveal an interesting aspect of many-body physics in 2D materials, our ARPES line-shape analysis can also provide a direct estimation of the hole carrier lifetime, an essential parameter for any valleytronics and spintronic applications. Our value (∼65 fs) is about two orders of magnitude lower than the theoretical estimation (∼4 ps) [52] for WS_2 ML where, however, only hole-electron and (neglibible) hole-phonon scattering processes are considered. In this context, our results suggest an important role played by intralayer defects of TMDC MLs in determining its final hole quasiparticle dynamics and transport properties.

IV. CONCLUSIONS

In this work we report an ARPES investigation of the electronic properties of the WS_2 ML/HOPG interface where the weak layer-substrate interaction facilitates a direct access of valley hole quasiparticle (and locked spin) dynamics in the WS_2 ML. At the valence band valley point our photoemission data show a clear asymmetry in the ARPES peak line shape, previously not resolved in ARPES studies of TMDC MLs. By temperature-dependent measurements, this peculiar spectral feature was analyzed and attributed to valley hole quasiparticle interaction with intralayer electrons and defects while negligible hole-phonon coupling was found. These results have major implications on the charge (and valley-locked spin) transport mechanism in semiconducting TMDC MLs suggesting, in good agreement with transport studies of TMDC MLs, a nearly temperature-independent hole mobility, as directly extracted from the line shape and band dispersion analysis. Our findings provide insights on the hole quasiparticle dynamics in TMDC MLs and support that such valley-locked holes could be advantageous for valleytronics and spintronic devices.

ACKNOWLEDGMENT

This work was supported by the Agency for Science, Technology and Research (A*STAR) under its A*STAR Pharos Grants No. 1527000016 and No. 1527000017 and A*STAR QTE Grant No. A1685b0005.

APPENDIX: METHODS

Sample preparation. The WS_2 ML was grown on a sapphire substrate using chemical vapor deposition in a commercially available quartz tube furnace (PlanarTECH LLC) at a temperature of 850 °C, at atmospheric pressure in a forming gas atmosphere [36]. We obtained large-area (mm-sized) sheets of monolayer WS_2 by careful optimization of the growth conditions and precursor concentrations. The WS_2 was then subsequently transferred onto a freshly cleaved HOPG substrate (SPI supplier, ZYA grade) by the use of a water-assisted transfer method with a PMMA/PDMS polymer stack [65]. After the transfer, the transfer polymer was cleaned off in acetone and isopropyl alcohol.

ARPES measurements. The ARPES data were acquired in a custom-designed system, with a hemispherical electron analyzer (SCIENTA DA30L) and monochromatized HeI_α ($h\nu = 21.218$ eV) radiation source (SCIENTA VUV5k). A schematic description of the experimental geometry and additional details on the system are provided in Sec. S1 and Fig. S1 in the SM.

XPS measurements. XPS data of WS_2 (ML)/HOPG were acquired with a hemispherical electron analyzer (SCIENTA HiPP-2) in normal emission condition, by using a

monochromatized Al K_α ($h\nu = 1486.6$ eV) as energy excitation source and energy resolution of 0.2 eV. More details about XPS measurements are included in Sec. S3 of the SM.

DFT calculations. All the band structure calculations were performed by using the plane-wave technique implemented in Vienna *ab initio* simulation package (VASP). [66] Grimme's DFT-D2 method has been applied to correct the insufficient description of vdW interactions in DFT [67,68]. The projector-augmented wave (PAW) method was applied to describe the electron-ion interaction, and the cutoff energy was set to 500 eV [69]. The free-standing ML valence band structures were calculated using the PBE functional [70] with spin-orbit coupling and in-plane lattice parameter $a = 3.16$ Å as-extracted by parabolic fitting at valence band dispersion around the K point (see the next subsection). The charge density of valence band states at the Γ point (VB^Γ) and local maxima at the K point (VB_1^K, VB_2^K) in Fig. 1(j) were calculated according to the above condition. Details on the impact of temperature induced structural change on the WS_2 are reported in Sec. S4 in the SM.

EDCs fitting. Experimental EDCs were fitted by a series of symmetric Voigt functions [47], i.e., convolution between Gaussian and a Lorentzian peak functions. ARPES data were integrated within ± 0.01 Å^{-1} around the K and Γ points, where no appreciable band dispersion was detected, to increase the signal-to-noise ratio. To simplify the theoretical analysis, the Voigt components around VB_1 and VB_2 local maxima were constrained to be equally spaced [energy separation $\Delta\varepsilon_1^K$, $\Delta\varepsilon_2^K$; Figs. 2(a) and 2(b)] and to have the same Gaussian w_G and Lorentzian w_L full width at half maximum (FWHM). FWHMs and energy separation were estimated with an uncertainty of ± 5 and ± 10 meV, respectively. Additional details on the fitting model are discussed in Sec. S6.

Parabolic fitting at K point: estimation of the in-plane lattice parameter and valley hole effective mass. The experimental binding energy of the VB_1 band as a function of $k_{//}$ was determined from the corresponding EDCs peak maxima positions, as extracted by peak fitting procedure (same as above). The uncertainty in the binding energy and momentum was ± 5 meV and ± 0.005 Å^{-1}, respectively. Note that as $k_{//}$ change across K, the valence-band dispersion along the ΓK direction of the first BZ and the KM band dispersion of the second BZ are effectively mapped. This is due to the "honeycomb" structure of the full hexagonal reciprocal space [see inset in Fig. 4(a)], which leads to a nonsymmetrical band dispersion across the K point. To minimize the impact of the band dispersion asymmetry on the momentum range around the maximum of fitting results, the parabolic fit was limited to ± 0.07 Å^{-1}.

A fitted momentum value of $k_{//}^K = (1.325 \pm 0.005)$ Å^{-1} was obtained for both 297 and 11 K. According to the hexagonal symmetry of the WS_2 unit cell system, the WS_2 in-plane lattice constant (a) and corresponding uncertainty (Δa) were obtained as $a = 4\pi/3k_{//}^K$ and $\Delta a = (4\pi/3k_{//}^{K^2})\Delta k_{//}^K$, respectively. A lattice constant $a = (3.16 \pm 0.01)$ Å of WS_2 ML was extracted at 297 and 11 K in line with the literature value [71].

The hole effective mass at the valley point was defined as $m^* = \hbar^2/C$, where $C = dE_{\text{Bin}}^2(k_{//})/d^2k_{//}$ is the curvature of the VB_1 band at the K point. The band curvature and corresponding uncertainty (ΔC) were extracted from the parabolic fitting of experimental data and the uncertainty in the hole effective mass was calculated as $\Delta m^* = (\hbar^2/C^2)\Delta C$.

[1] D. Xiao, G.-B. Liu, W. Feng, X. Xu, and W. Yao, Phys. Rev. Lett. **108**, 196802 (2012).
[2] J. R. Schaibley, H. Yu, G. Clark, P. Rivera, J. S. Ross, K. L. Seyler, W. Yao, and X. Xu, Nat. Rev. Mater. **1**, 16055 (2016).
[3] K. F. Mak, K. He, J. Shan, and T. F. Heinz, Nat. Nanotechnol. **7**, 494 (2012).
[4] G. Wang, X. Marie, B. L. Liu, T. Amand, C. Robert, F. Cadiz, P. Renucci, and B. Urbaszek, Phys. Rev. Lett. **117**, 187401 (2016).
[5] C. Mai, A. Barrette, Y. Yu, Y. G. Semenov, K. W. Kim, L. Cao, and K. Gundogdu, Nano Lett. **14**, 202 (2014).
[6] N. W. Ashcroft and N. D. Mermin, *Solid State Physics* (Holt, Rinehart and Winston, New York, 1976).
[7] W. Han, APL Mater. **4**, 032401 (2016).
[8] F. Bussolotti, H. Kawai, Z. E. Ooi, V. Chellappan, D. Thian, A. L. C. Pang, and K. E. J. Goh, Nano Futur. **2**, 032001 (2018).
[9] M. Amani, M. L. Chin, A. G. Birdwell, T. P. O'Regan, S. Najmaei, Z. Liu, P. M. Ajayan, J. Lou, and M. Dubey, Appl. Phys. Lett. **102**, 193107 (2013).
[10] W. Liu, J. Kang, D. Sarkar, Y. Khatami, D. Jena, and K. Banerjee, Nano Lett. **13**, 1983 (2013).
[11] Y. Liu, J. Guo, E. Zhu, L. Liao, S. J. Lee, M. Ding, I. Shakir, V. Gambin, Y. Huang, and X. Duan, Nature (London) **557**, 696 (2018).
[12] B. Radisavljevic, A. Radenovic, J. Brivio, V. Giacometti, and A. Kis, Nat. Nanotechnol. **6**, 147 (2011).
[13] A. Allain and A. Kis, ACS Nano **8**, 7180 (2014).
[14] D. Ovchinnikov, A. Allain, Y. S. Huang, D. Dumcenco, and A. Kis, ACS Nano **8**, 8174 (2014).
[15] E. Ponomarev, Á. Pásztor, A. Waelchli, A. Scarfato, N. Ubrig, C. Renner, and A. F. Morpurgo, ACS Nano **12**, 2669 (2018).
[16] Y. Zhang, T. R. Chang, B. Zhou, Y. T. Cui, H. Yan, Z. Liu, F. Schmitt, J. Lee, R. Moore, Y. Chen, H. Lin, H. T. Jeng, S. K. Mo, Z. Hussain, A. Bansil, and Z. X. Shen, Nat. Nanotechnol. **9**, 111 (2014).
[17] D. N. Basov, M. M. Fogler, A. Lanzara, F. Wang, and Y. Zhang, Rev. Mod. Phys. **86**, 959 (2014).
[18] T. Valla, A. V. Fedorov, P. D. Johnson, and S. L. Hulbert, Phys. Rev. Lett. **83**, 2085 (1999).
[19] A. Damascelli, Z. Hussain, and Z. X. Shen, Rev. Mod. Phys. **75**, 473 (2003).
[20] G. Nicolay, B. Eltner, S. Hüfner, F. Reinert, U. Probst, and E. Bucher, Phys. Rev. B **73**, 045116 (2006).
[21] W. Jin, P.-C. Yeh, N. Zaki, D. Zhang, J. T. Sadowski, A. Al-Mahboob, A. M. van der Zande, D. A. Chenet, J. I. Dadap, I. P. Herman, P. Sutter, J. Hone, and R. M. Osgood, Jr., Phys. Rev. Lett. **111**, 106801 (2013).

[22] W. Jin, P. C. Yeh, N. Zaki, D. Zhang, J. T. Liou, J. T. Sadowski, A. Barinov, M. Yablonskikh, J. I. Dadap, P. Sutter, I. P. Herman, and R. M. Osgood, Phys. Rev. B **91**, 121409(R) (2015).

[23] N. Alidoust, G. Bian, S.-Y. Xu, R. Sankar, M. Neupane, C. Liu, I. Belopolski, D.-X. Qu, J. D. Denlinger, F.-C. Chou, and M. Z. Hasan, Nat. Commun. **5**, 4673 (2014).

[24] H. Henck, Z. Ben Aziza, D. Pierucci, F. Laourine, F. Reale, P. Palczynski, J. Chaste, M. G. Silly, F. Bertran, P. Le Fèvre, E. Lhuillier, T. Wakamura, C. Mattevi, J. E. Rault, M. Calandra, and A. Ouerghi, Phys. Rev. B **97**, 155421 (2018).

[25] N. F. Hinsche, A. S. Ngankeu, K. Guilloy, S. K. Mahatha, A. Grubišić Čabo, M. Bianchi, M. Dendzik, C. E. Sanders, J. A. Miwa, H. Bana, E. Travaglia, P. Lacovig, L. Bignardi, R. Larciprete, A. Baraldi, S. Lizzit, K. S. Thygesen, and P. Hofmann, Phys. Rev. B **96**, 121402(R) (2017).

[26] A. Bruix, J. A. Miwa, N. Hauptmann, D. Wegner, S. Ulstrup, S. S. Grønborg, C. E. Sanders, M. Dendzik, A. Grubišić Čabo, M. Bianchi, J. V. Lauritsen, A. A. Khajetoorians, B. Hammer, and P. Hofmann, Phys. Rev. B **93**, 165422 (2016).

[27] Y. Zhang, M. M. Ugeda, C. Jin, S.-F. Shi, A. J. Bradley, A. Martín-Recio, H. Ryu, J. Kim, S. Tang, Y. Kim, B. Zhou, C. Hwang, Y. Chen, F. Wang, M. F. Crommie, Z. Hussain, Z.-X. Shen, and S.-K. Mo, Nano Lett. **16**, 2485 (2016).

[28] See Supplemental Material at http://link.aps.org/supplemental/10.1103/PhysRevB.103.045412 for additional experimental and theoretical details.

[29] F. Bussolotti, Z. Zhang, H. Kawai, and K. E. J. Goh, MRS Adv. **2**, 1527 (2017).

[30] F. Bussolotti, H. Kawai, S. L. Wong, and K. E. J. Goh, Phys. Rev. B **99**, 045134 (2019).

[31] S.-K. Mo, C. Hwang, Y. Zhang, M. Fanciulli, S. Muff, J. Hugo Dil, Z.-X. Shen, and Z. Hussain, J. Phys.: Condens. Matter **28**, 454001 (2016).

[32] J. A. Miwa, M. Dendzik, S. S. Grønborg, M. Bianchi, J. V Lauritsen, P. Hofmann, and S. Ulstrup, ACS Nano **9**, 6502 (2015).

[33] M. Dendzik, M. Michiardi, C. Sanders, M. Bianchi, J. A. Miwa, S. S. Grønborg, J. V. Lauritsen, A. Bruix, B. Hammer, and P. Hofmann, Phys. Rev. B **92**, 245442 (2015).

[34] D. A. Shirley, Phys. Rev. B **5**, 4709 (1972).

[35] C. D. Wagner and G. E. Muilenberg, *Handbook of X-Ray Photoelectron Spectroscopy: A Reference Book of Standard Data for Use in x-Ray Photoelectron Spectroscopy* (Perkin-Elmer, Eden Prairie, 1979).

[36] K. M. McCreary, A. T. Hanbicki, G. G. Jernigan, J. C. Culbertson, and B. T. Jonker, Sci. Rep. **6**, 19159 (2016).

[37] C. Kastl, R. J. Koch, C. T. Chen, J. Eichhorn, S. Ulstrup, A. Bostwick, C. Jozwiak, T. R. Kuykendall, N. J. Borys, F. M. Toma, S. Aloni, A. Weber-Bargioni, E. Rotenberg, and A. M. Schwartzberg, ACS Nano **13**, 1284 (2019).

[38] J. Hong, Z. Hu, M. Probert, K. Li, D. Lv, X. Yang, L. Gu, N. Mao, Q. Feng, L. Xie, J. Zhang, D. Wu, Z. Zhang, C. Jin, W. Ji, X. Zhang, J. Yuan, and Z. Zhang, Nat. Commun. **6**, 6293 (2015).

[39] R. Soklaski, Y. Liang, and L. Yang, Appl. Phys. Lett. **104**, 193110 (2014).

[40] P. A. Young, J. Phys. D: Appl. Phys. **1**, 936 (1968).

[41] C. K. Gan and Y. Y. F. Liu, Phys. Rev. B **94**, 134303 (2016).

[42] D. Zhang, Y. C. Wu, M. Yang, X. Liu, C. Coileáin, H. Xu, M. Abid, M. Abid, J. J. Wang, I. V. Shvets, H. Liu, Z. Wang, H. Yin, H. Liu, B. S. Chun, X. Zhang, and H. C. Wu, RSC Adv. **6**, 99053 (2016).

[43] M. M. Ugeda, A. J. Bradley, S. F. Shi, F. H. Da Jornada, Y. Zhang, D. Y. Qiu, W. Ruan, S. K. Mo, Z. Hussain, Z. X. Shen, F. Wang, S. G. Louie, and M. F. Crommie, Nat. Mater. **13**, 1091 (2014).

[44] M. Okada, A. Kutana, Y. Kureishi, Y. Kobayashi, Y. Saito, T. Saito, K. Watanabe, T. Taniguchi, S. Gupta, Y. Miyata, B. I. Yakobson, H. Shinohara, and R. Kitaura, ACS Nano **12**, 2498 (2018).

[45] D. Pierucci, H. Henck, J. Avila, A. Balan, C. H. Naylor, G. Patriarche, Y. J. Dappe, M. G. Silly, F. Sirotti, A. T. C. Johnson, M. C. Asensio, and A. Ouerghi, Nano Lett. **16**, 4054 (2016).

[46] S.M. Sze, *Physics of Semiconductor Devices* (Wiley and Sons, New York, 2002).

[47] M. Cardona and L. Ley, *Photoemission in Solids I—General Principles* (Springer, Berlin, 1978).

[48] S. Tougaard, J. Electron. Spectrosc. Relat. Phenom. **178–179**, 128 (2010).

[49] M. P. Seah and W. A. Dench, Surf. Interface Anal. **1**, 2 (1979).

[50] K. M. Shen, F. Ronning, D. H. Lu, W. S. Lee, N. J. C. Ingle, W. Meevasana, F. Baumberger, A. Damascelli, N. P. Armitage, L. L. Miller, Y. Kohsaka, M. Azuma, M. Takano, H. Takagi, and Z. X. Shen, Phys. Rev. Lett. **93**, 267002 (2004).

[51] W. Chen, G. Khaliullin, and O. P. Sushkov, Phys. Rev. B **80**, 094519 (2009).

[52] C. J. Ciccarino, T. Christensen, R. Sundararaman, and P. Narang, Nano Lett. **18**, 5709 (2018).

[53] Z. Jin, X. Li, J. T. Mullen, and K. W. Kim, Phys. Rev. B **90**, 045422 (2014).

[54] M. L. Trolle, T. G. Pedersen, and V. Véniard, Sci. Rep. **7**, 39844 (2017).

[55] A. Raja, A. Chaves, J. Yu, G. Arefe, H. M. Hill, A. F. Rigosi, T. C. Berkelbach, P. Nagler, C. Schüller, T. Korn, C. Nuckolls, J. Hone, L. E. Brus, T. F. Heinz, D. R. Reichman, and A. Chernikov, Nat. Commun. **8**, 15251 (2017).

[56] J. Katoch, S. Ulstrup, R. J. Koch, S. Moser, K. M. McCreary, S. Singh, J. Xu, B. T. Jonker, R. K. Kawakami, A. Bostwick, E. Rotenberg, and C. Jozwiak, Nat. Phys. **14**, 355 (2018).

[57] L. Waldecker, A. Raja, M. Rösner, C. Steinke, A. Bostwick, R. J. Koch, C. Jozwiak, T. Taniguchi, K. Watanabe, E. Rotenberg, T. O. Wehling, and T. F. Heinz, Phys. Rev. Lett. **123**, 206403 (2019).

[58] S. Ulstrup, C. E. Giusca, J. A. Miwa, C. E. Sanders, A. Browning, P. Dudin, C. Cacho, O. Kazakova, D. K. Gaskill, R. L. Myers-Ward, T. Zhang, M. Terrones, and P. Hofmann, Nat. Commun. **10**, 3283 (2019).

[59] C. Kim, I. Moon, D. Lee, M. S. Choi, F. Ahmed, S. Nam, Y. Cho, H. J. Shin, S. Park, and W. J. Yoo, ACS Nano **11**, 1588 (2017).

[60] F. Rittweger, N. F. Hinsche, and I. Mertig, J. Phys.: Condens. Matter **29**, 355501 (2017).

[61] N. R. Wilson, P. V. Nguyen, K. Seyler, P. Rivera, A. J. Marsden, Z. P. L. Laker, G. C. Constantinescu, V. Kandyba, A. Barinov, N. D. M. Hine, X. Xu, and D. H. Cobden, Sci. Adv. **3**, e1601832 (2017).

[62] J. W. Gadzuk and M. Sunjic, Phys. Rev. B **12**, 524 (1975).
[63] S. Doniach and M. Sunjic, J. Phys. C: Solid State Phys. **3**, 285 (1969).
[64] B. Zhu, X. Chen, and X. Cui, Sci. Rep. **5**, 9218 (2015).
[65] H. Li, J. Wu, X. Huang, Z. Yin, J. Liu, and H. Zhang, ACS Nano **8**, 6563 (2014).
[66] G. Kresse and J. Hafner, Phys. Rev. B **47**, 558(R) (1993).
[67] S. Grimme, J. Comput. Chem. **27**, 1787 (2006).
[68] L.-Y. Gan, Y.-J. Zhao, D. Huang, and U. Schwingenschlögl, Phys. Rev. B **87**, 245307 (2013).
[69] P. E. Blochl, Phys. Rev. B **50**, 17953 (1994).
[70] J. P. Perdew, K. Burke, and M. Ernzerhof, Phys. Rev. Lett. **77**, 3865 (1996).
[71] A. Molina-Sánchez and L. Wirtz, Phys. Rev. B **84**, 155413 (2011).

Correction: An inline equation in the seventh sentence of the paragraph of Sec. II C contained an error and has been fixed.